

Photo-Fenton performance and mechanism of g-C₃N₄/FeOCl nanocomposite under simulate sunlight

Jinhuan Ma (✉ jhma123654@163.com)

Lanzhou University of Technology

Zhiqiang Wei

Lanzhou University of Technology <https://orcid.org/0000-0002-1173-9412>

Qiang Lu

Lanzhou University of Technology

Chao Li

Lanzhou University of Technology

Ling Li

Lanzhou University of Technology

Research Article

Keywords: g-C₃N₄, FeOCl, Z-type heterojunction, photo-Fenton Mechanism, Driving H₂O₂

Posted Date: February 2nd, 2022

DOI: <https://doi.org/10.21203/rs.3.rs-1113780/v1>

License:   This work is licensed under a Creative Commons Attribution 4.0 International License.

[Read Full License](#)

Abstract

g-C₃N₄/FeOCl nanocomposites are prepared by a simple calcination method according to the different composite mass ratios of g-C₃N₄ and FeOCl. The microstructure and morphology were characterized by X-ray diffraction (XRD), field emission scanning electron microscopy (FESEM), high-resolution transmission electron microscopy (HRTEM). It is found that the composite samples are mainly composed of FeOCl phase, and the presence of g-C₃N₄, indicating the successful composite of the sample without destroying the crystal structure of FeOCl. Through Electrochemical impedance spectroscopy (EIS) and transient photocurrent response, it is found that the photoelectrochemical performance of the composite sample g-C₃N₄/FeOCl-2 is stronger than that of pure FeOCl. In addition, through photo-Fenton and radical-trapping experiments, it is found that g-C₃N₄/FeOCl-2 degrades 92% of Rhodamine B (RhB) within 90 min, and ·OH radicals play an important role in the process of photo-Fenton degradation. The enhanced photocatalytic performance is mainly ascribed to the Z-type heterojunctions between FeOCl and g-C₃N₄, preventing the recombination of photogenerated electrons and holes, and improving the absorption efficiency of natural light. In this work, the high-efficiency photo-Fenton performance of g-C₃N₄/FeOCl-2 provides a new idea about the modification of pure FeOCl.

1 Introduction

In recent decades, with the development of society and the rapid growth of population, more and more countries have begun to pay attention to environmental governance, especially the control of water pollution has always been the top priority because water is one of the indispensable resources for the survival of life on earth (Li et al., 2021; J. H. Ma et al., 2021). In order to overcome the crisis of severe water shortage, the advanced oxidation process has become a powerful solution for water pollution control because of its high efficiency, environmental protection, and no secondary pollution (Amor et al., 2015; Wei et al., 2020). It has also attracted significant attention from scholars at home and abroad (Zhu et al., 2021). Fenton reaction and photocatalytic reaction are two outstanding representatives in the advanced oxidation process, especially photo-Fenton oxidation (Yao et al., 2019). However, is limited by the sluggish reaction kinetics of Fe³⁺ and H₂O₂.

Ferric oxychloride (FeOCl) is a known high-efficiency iron-based heterogeneous Fenton catalyst, which has shown much better FeOCl shows extremely high efficiency in driving H₂O₂ to decompose into ·OH via the Fe³⁺/Fe²⁺ redox cycle than other iron compounds (Pan et al., 2021; S. Y. Qu et al., 2020). The excellent photo-Fenton activity is attributed to the unique 2-dimensional layered structure of FeOCl and the reducible electronic properties of iron atoms because the unique Fe-O-Fe and O-Fe-Cl linear structures of the unsaturated iron atoms exposed on the surface of FeOCl (Fig. 1 (a)) (M. D. Chen et al., 2018; Y. P. Ma et al., 2021). As shown of Fig. 1 (b), FeOCl was activating H₂O₂. However, owing to FeOCl was a narrow bandgap semi (1.8 eV), the recombination rate of the photogenerated electron-hole pairs was low (Sabri et al., 2020). To overcome this shortcoming, construction of heterojunctions between FeOCl and another semiconductor to improve its ability that generated photogenerated electron-hole pairs, thereby improving

the photo-Fenton performance of FeOCl (Luo et al., 2021). For example, FeOCl/SiO₂ and FeOCl/MoS₂ composites were recently reported to prove the FeOCl materials with constructed of heterojunctions could expose more active sites, which leads to the improvement of the photo-Fenton performance of the entire system (Liu et al., 2021; Yang et al., 2016).

As an n-type metal-free polymer, g-C₃N₄ has gradually become a research hotspot that it has the advantages of non-toxicity, low cost, high stability, and simple preparation method (Li et al., 2019; V. H. Nguyen et al., 2021). g-C₃N₄, which is also of a wide bandgap (2.7 eV), the low quantum efficiency and fast recombination rate of photogenerated carriers results in pure g-C₃N₄, which limits its industrial application (Asadzadeh-Khaneghah et al., 2021; L. H. Qu et al., 2020). In order to overcome the limitation of the bandgap of g-C₃N₄, the most usually used method is to use the wide bandgap of g-C₃N₄ to form a heterojunction with other semiconductors, lead to increase the rate of photo-generated carriers and enhance the photosensitization performance of the catalyst (Li et al., 2014). However, many methods have been utilized to enhance photocatalytic activity, such as metal doping, defect generation, morphological adjustment, noble metal deposition, and heterojunction construction (T. T. H. Nguyen et al., 2021; Zeng et al., 2019).

In this work, g-C₃N₄/FeOCl heterojunctions with different mass ratios were successfully fabricated by a simple calcination method for advanced photoelectrochemical performance and degradation efficiency. And the microstructure, morphology, photoelectrochemical and photocatalytic properties of the samples were characterized by X-ray diffraction (XRD), scanning electron microscopy (SEM), high-resolution transmission electron microscopy (HRTEM), energy-dispersive X-ray spectroscopy (EDX), X-ray photoelectron spectrometer (XPS), Fourier transform infrared spectra (FT-IR) and UV-vis diffuse reflection spectroscopy (UV-vis DRS). Electrochemical impedance spectroscopy (EIS) and transient photocurrent response were tested to evaluate the photogenerated charges recombination and electron transportation performance. The effects of the composite ratio on the photo-Fenton performance of the samples were evaluated by the photo-Fenton degradation of RhB in aqueous solution under the simulated sunlight, and the possible enhanced visible photo-Fenton activity mechanism was also proposed.

2. Materials And Methods

2.1 Synthesis of g-C₃N₄ materials

g-C₃N₄ powder is synthesized by a simple calcination method. Firstly, weigh a certain amount of melamine (analytical grade), grind and place it flat on the bottom of the crucible, put it into the tube furnace, which raises to 550°C with a temperature of 5°C/min in the air, and kept it heat for two hours. Then it is naturally cooled to room temperature to obtain a light yellow powder.

2.2 Preparation of FeOCl samples

FeOCl material is synthesized by a simple calcination method. A certain amount of $\text{FeCl}_3 \cdot 6\text{H}_2\text{O}$ (analytical purity) solid was ground in a mortar for 30 min, and then heat at 250°C for 1 h in air. After being naturally cooled to room temperature, washing with acetone several times to remove excess FeCl_3 , and then dry in an oven at 60°C for 10 hours. Then the dark purple powder obtained is FeOCl material.

2.3. Preparation of $\text{g-C}_3\text{N}_4/\text{FeOCl}$ nanocomposites

The synthesis method of $\text{g-C}_3\text{N}_4/\text{FeOCl}$ composite material is the same as that of pure FeOCl material. The prepared $\text{g-C}_3\text{N}_4$ and $\text{FeCl}_3 \cdot 6\text{H}_2\text{O}$ solids were mixed at different mass ratios of 1:15, 1:20, and 1:25, respectively. Then the mixture was milled for 30 min and calcined at 250°C for 1 h, naturally cooled to room temperature, washed with acetone several times to remove excess FeCl_3 , and then drying 60°C for 10 h in drying cabinet. The prepared powders were named $\text{g-C}_3\text{N}_4/\text{FeOCl-1}$, $\text{g-C}_3\text{N}_4/\text{FeOCl-2}$ and $\text{g-C}_3\text{N}_4/\text{FeOCl-3}$, respectively.

2.4. Photocatalytic activity measurement and active species capture experiment

The photo-Fenton experiment uses 100 mL RhB, the initial concentration is 10 mg/L, and the photocatalyst is 0.01 g. Adjust the initial pH of the dye solution by using 0.1 mol/L hydrochloric acid (HCl) and 0.1 mol/L Sodium Hydroxide (NaOH). At the same time, the catalyst was added to the RhB solution, and adjusted pH=6~7, and stirring was continued for 30 min to reach the absorption-desorption equilibrium. Subsequently, 0.4 mL H_2O_2 was added, and visible light was irradiated on the suspension immediately. Take out a small amount of solution every 30 min to measure the concentration of RhB. Use a visible spectrophotometer ($\lambda = 554 \text{ nm}$) to test the absorbance of the solution. The Lambert-Beer law defines the degradation rate: $(C_t - C_0)/C_0 \times 100\% = (A - A_{0t})/A_0 \times 100\%$, where C_0 and C_t represent the initial solution concentration. After exposure time t , A_0 and A_t respectively is the corresponding absorbance of the solution. In the radical-trapping experiment, p-benzoquinone (BQ), Methanol (IA), and isopropanol (IPA) were used as capture agents for $\cdot\text{O}_2^-$, h^+ , and $\cdot\text{OH}$ respectively.

3. Results And Discussion

3.1. Structure and morphology analysis

The typical XRD patterns of pure FeOCl, pure $\text{g-C}_3\text{N}_4$ and $\text{g-C}_3\text{N}_4/\text{FeOCl}$ nanocomposites with different mass ratios are shown in Fig. 1. It is obvious that that pure $\text{g-C}_3\text{N}_4$ displays one characteristic peak at $2\theta = 27.5^\circ$, which are associated with (002) diffraction planes of $\text{g-C}_3\text{N}_4$. For pure FeOCl, the diffraction peaks at peaks appear at $2\theta = 11.16^\circ, 26.10^\circ, 35.37^\circ, 37.89^\circ, 48.10^\circ$, and 61.10° , which exactly assigned to the crystal planes (010), (110), (021), (111), (200), and (221) of the hexagonal structure of FeOCl with JPCDS (No.72-0619), respectively. The characteristic peak shape of FeOCl is sharp and the intensity is high from the figure, indicating that the prepared FeOCl material has a complete crystal form and high crystallinity. In addition, the diffraction peaks of $\text{g-C}_3\text{N}_4/\text{FeOCl}$ nanocomposites with different mass

ratios are consistent with pure FeOCl, with the introduction of g-C₃N₄, no obvious g-C₃N₄ diffraction peak is observed, which may be attributed to the strong interaction between FeOCl and g-C₃N₄, resulting in the predominant (002) diffraction peak of g-C₃N₄ ($2\theta = 27.5^\circ$) coincides with the peak at 26.10° of FeOCl. Compared with pure FeOCl, no other impure peaks are observed for g-C₃N₄/FeOCl composites, indicating that the g-C₃N₄/FeOCl samples have been successfully synthesized.

The features of the as-synthesized photocatalysts were examined using SEM and HRTEM. From Fig. 3 (a, b), it is clear that the shape of pure FeOCl mainly exhibits the layered structure of cuboid nanorods, the average thickness of the nanorod structure is about from 300 to 400 nm. Fig. 3 (c), the HRTEM image of g-C₃N₄/FeOCl-2 calculates the characteristic d spacing as 0.275 nm and 0.236 nm are assigned to (120) and (111) plane of FeOCl. Fig. 3(d), the selected area electron diffraction of g-C₃N₄/FeOCl-20 shows that there are five obvious diffraction rings respectively corresponding to several representative crystal planes of FeOCl (110), (210), (200), (002), (152), indicating that the crystallinity of the composite sample has not decreased.

As shown in Fig. 4 (a), irregular black long strips are stacked together, covered with a thin layer of transparent yarn-like substance, indicating the successful synthesis of g-C₃N₄/FeOCl-2 nanocomposite. In Fig. 4 (b) shows the EDX spectra of g-C₃N₄/FeOCl-2 nanocomposites. It can be seen g-C₃N₄/FeOCl-2 nanocomposites only contain C, N, O, Cl, and Fe elements characteristic peaks. And the atomic percentage and weight percentage of related elements of the g-C₃N₄/FeOCl-2 nanocomposite are almost close to the nominal stoichiometry used in their respective precursors, without any impurity elements introduced. In addition, from Fig. 4 (c-h) TEM-mapping can be seen that the Fe, O, Cl, C, and N elements are distributed very uniformly, indicating that the g-C₃N₄/FeOCl-2 prepared by this method has high purity and compact structure.

3.2 XPS analysis

Fig. 5 (a) is the XPS full spectrum of g-C₃N₄/FeOCl-2 material. The peaks of Fe, O, Cl, C, and N elements can be clearly observed in the XPS full spectrum, indicating Fe, O, Cl, C, and N elements existed in the g-C₃N₄/FeOCl-2 material. In Fig. 5 (b), The binding energies of 2p_{3/2} and 2p_{1/2} of Fe are 708.7 and 722.4 eV, respectively (Y. Q. Chen et al., 2018). Among them, the characteristic peak corresponding to the binding energy at 708.7 eV is Fe (II) 2p_{3/2} (Luo et al., 2019), which indicates that in addition to Fe(III) in the FeOCl sample, there is also a small amount of Fe(II). Fig. 5 (c) shows that the binding energies of O 1s are 527.5 and 530.2 eV, one peak at 527.5 eV is considered to be O attached to the metal (Fe-O), while the other at 530.2 eV is attributable to O adsorbed on the H₂O molecule on the catalyst surface. Fig. 3 (d) shows that the binding energies of Cl 2p are 195.2 and 197.8 eV corresponding to the Fe-Cl bond of FeOCl. Fig. 5 (e) the binding energies of C1s are 286.1 and 281.3 eV, comes from sp² N-C and sp² C-C bond, respectively (Ma et al., 2017). In Fig. 5 (f), the peak at 398.2 eV was allocated to N element in tertiary N (N-C) (Asadzadeh-Khaneghah et al., 2018).

3.3. UV-vis DRS and FT-IR analysis

UV-vis DRS to test the visible light absorption characteristics and energy band structure of pure g-C₃N₄, FeOCl, and composite g-C₃N₄/FeOCl. As seen from Fig. 6(a), the visible light response range of bare g-C₃N₄ was 250–456 nm. Compared with pure g-C₃N₄, the light response range of pure FeOCl and composite g-C₃N₄/FeOCl both presented broad absorption over the whole region from 250 to 685 nm. Moreover, the absorption edges of g-C₃N₄/FeOCl-1, g-C₃N₄/FeOCl-2, and g-C₃N₄/FeOCl-3 nanocomposites are approximately located at 684, 685, and 676 nm in the visible light region, respectively. The visible light response range of the g-C₃N₄/FeOCl nanocomposite hasn't changed than pure FeOCl, indicating that the introduction of g-C₃N₄ has little response to changing the visible light of the FeOCl. The bandgaps were also estimated using the model proposed by Tauc: $(\alpha hv)^{1/n} = A(hv - Eg)$ (Fig. 6(b)) (Huang et al., 2021; Varaprasad et al., 2021), the band gaps of g-C₃N₄ and FeOCl were 2.72 and 1.82 eV, respectively. And The bandgap of g-C₃N₄/FeOCl sample is basically the same as that of pure FeOCl. It shows that there is no obvious blueshift and redshift in the composite sample.

FT-IR analysis was used to characterize the information of chemical bonds and functional groups in the nanocomposites. As demonstrated in Fig. 7 broad band was observed at 3300 cm⁻¹ in the spectrum belongs to the O–H of the H₂O molecules that adsorbed on the surface of the material. At the position of 1200~1600 cm⁻¹ of the peaks was from the C–N and C=N bonds in g-C₃N₄ (Ren et al., 2015). The Fe–O bond displays the absorption band at 811.2 cm⁻¹ in the g-C₃N₄/FeOCl-2 system, indicating that there is not only the characteristic peak of g-C₃N₄ (Qu et al., 2019). Hence, the FT-IR measurement revealed the existence of g-C₃N₄, and FeOCl of functional groups in the g-C₃N₄/FeOCl-2 system, which is consistent with the results of XPS analysis.

3.4. Photoelectrochemical analysis

To investigate the photogenerated charge carrier transfer dynamics by measuring electrochemical impedance spectroscopy (EIS) and transient photocurrent spectra. As well known, the radius of the arc in the EIS plots corresponds to the separation efficiency of photogenerated electron-hole pairs, the arc radius is smaller that meant the better the separation effect of electron-hole pairs to lead to the better the photocatalytic performance. As exhibited in Fig. 8 (a), it can be clearly seen that the arc radius of g-C₃N₄/FeOCl-2 is the smallest, suggesting that the electron-hole pair separation effect of g-C₃N₄/FeOCl-2 is stronger than pure FeOCl and g-C₃N₄. Therefore, a higher high-speed charge carrier transfer at the g-C₃N₄/FeOCl-2 electrodes. The transient photocurrent test is to detect the number of photogenerated electron-hole pairs generated on the surface of the catalyst. The stronger the photocurrent intensity, the more photogenerated electrons are generated. In Fig. 8 (b) show the increased transient photocurrent of g-C₃N₄/FeOCl-2 compared with pure FeOCl, indicating that the compound with g-C₃N₄ can promote the separation of e⁻ and h⁺ of FeOCl.

The type of semiconductor and flat-band potential can be measured by the Mott-Schottky test. From Fig. 9(a, b), it can be seen that the slopes of the Schottky curve of the FeOCl and g-C₃N₄ are positive slope, which implied that both FeOCl and g-C₃N₄ are n-type semiconductors. According to electrochemical measurements of calomel electrodes at 3000 Hz and 5000 Hz, the flat band potentials of FeOCl and g-C₃N₄ are +0.037 V and -1.023 V vs SCE, respectively. Then, the measured flat band potentials vs SCE were converted to the normal hydrogen electrode (NHE) scale by $E_{\text{NHE}} = E_{\text{SCE}} + 0.059\text{pH} + 0.242(\text{pH}=7)$ (Li et al., 2021). It was known that the flat band potential of an n-type semiconductor is approximately equal to CB. The CB position of FeOCl and g-C₃N₄ could be calculated to be +0.692 and -0.368 V. It can be calculated that the valence band (VB) energy levels of FeOCl and g-C₃N₄ were +2.512 and +2.352 eV by the empirical formula $E_{\text{CB}} = E_{\text{VB}} - E_{\text{g}}$ (Zheng & Zhang, 2018).

3.5 Photocatalytic activity and Radical-trapping experiment

The photo-Fenton catalytic activity of g-C₃N₄, FeOCl, and g-C₃N₄/FeOCl samples was verified by degrading RhB solution in 90min (Fig. 10). All of the experiments were conducted by adding 0.4 mL H₂O₂ and the scale of pH=6~7. According to the results, FeOCl and g-C₃N₄ have lower RhB removal under dark conditions compared with composite samples, indicating relatively poor adsorption efficiency of RhB on the as-prepared pure FeOCl and g-C₃N₄. Under 90 minutes of light, the degradation rates of g-C₃N₄/FeOCl-1, g-C₃N₄/FeOCl-2, g-C₃N₄/FeOCl-3 nanocomposite are 80.7%, 92.2% and 88.0% respectively. However, the removal rates of pure FeOCl and g-C₃N₄ are 86.7% and 45.1%. The ability of the composite material to degrade pollutants is significantly improved. g-C₃N₄ is attached to the surface of the long FeOCl, and the full contact between the two forms a Z-type heterojunction (Zhao et al., 2020). Promote the migration and separation of photo-generated carriers.

In order to explore the photo-Fenton active materials of the g-C₃N₄/FeOCl-2/vis/H₂O₂ system, which was added active materials capture agents such as isopropanol (IPA), methanol (IA) and benzoquinone (BQ) by radical-trapping experiment (Fig. 11(a)). The degradation rate of RhB was significantly reduced after adding IPA in the suspension. And h⁺ also inhibited the progress of the experiment because h⁺ could capture enough H₂O to produce ·OH. The degradation rate of RhB didn't significantly change after adding BQ in the suspension, showing that the photo-induced ·O₂⁻ little influenced the degradation of RhB from Fig. 11(b). The radical-trapping experiment results demonstrate that ·OH plays a most important role, h⁺ is secondary species, and ·O₂⁻ also participated in the degradation of RhB.

3.6 Photocatalytic mechanism

Combining the above results, both g-C₃N₄ and FeOCl were n-type semiconductors and the CB and VB energy levels of FeOCl are higher than g-C₃N₄. Hence, the recombination of g-C₃N₄ and FeOCl would form a Z-type heterojunction. When the g-C₃N₄ and FeOCl contacted, electrons would spontaneously diffuse from g-C₃N₄ with a high Fermi level to the FeOCl from in Fig. 12 (a) (Yang, 2021). At the same time, a built-in electric field will be formed at the interface and the CB and VB of g-C₃N₄ and FeOCl would move

which was forming a side of heterojunction, eventually reaching a state of thermal equilibrium. The photo-Fenton mechanism diagram of g-C₃N₄/FeOCl could be drawn that when sunlight irradiates the surface of the catalyst, the CB and VB of g-C₃N₄ and FeOCl would produce non-equilibrium carrier electron-hole pairs. The heterojunction of g-C₃N₄/FeOCl and the state of thermal equilibrium were broken. The CB of FeOCl electrons migrated to the VB of g-C₃N₄ to recombine with holes, which the electrons were gathered on the CB of g-C₃N₄ and a large number of holes produced on the VB of FeOCl.

According to Fig. 12 (b), H₂O₂ was converted ·OH and OH⁻ by the electrons that gathered at the CB of g-C₃N₄, the VB of FeOCl h⁺ captured H₂O to convert ·OH. During this process, the H₂O₂ and H₂O were served as the electron and hole acceptors which the recombination of holes and electrons further were successfully limited (Xing et al., 2020). On the other hand, on the surface Fe³⁺ of FeOCl material transformed into the Fe²⁺ with the existence of H₂O₂ under the radiation of sunlight condition, and the Fe²⁺ was easily reacted with H₂O₂ to generated the ·OH (Ye et al., 2018). In addition, owing to Standard reduction potential (E⁰(O₂/·O₂⁻)) was more positive than the CB of g-C₃N₄ and Standard oxidation potential (E⁰(·OH/OH⁻)) was more negative than the VB of FeOCl, the electron on the CB of the g-C₃N₄ would also reduce O₂ to form the ·O₂⁻ and the h⁺ which produced on the VB of the FeOCl could oxide the ·OH⁻ into the ·OH (Chen et al., 2020). Based on the radical-trapping experiment obtained the possible photo-Fenton degradation mechanism.

4. Conclusion

In this study, all materials were both prepared by a simple calcination method. the metal-free polymer g-C₃N₄ was introduced by forming the Z-type heterojunction with FeOCl, which effectively limited the recombination of electron-hole pairs. In the Fe-based photo-Fenton system, calculated the degradation rate of RhB under a condition of 0.01g catalyst, 0.4mL H₂O₂ (30%), and the initial concentration of RhB of 10 mg/L. The results show that g-C₃N₄/FeOCl-2 can efficiently degrade RhB solution which had an excellent photo-Fenton performance. Besides, H₂O₂ provided active substances he circulation between Fe³⁺/Fe²⁺ in the system, as well as provides enough ·OH for the degradation of pollutants.

Declarations

- **Ethics approval** Not applicable.
- **Consent to participate** Not applicable.
- **Consent for publication** All authors agree to publish.
- **Availability of data and materials** Not applicable.
- **Competing interests** The authors declare no competing interests.
- **Funding** This work was supported by the National Natural Science Foundation of

- China (51261015). This work was supported by the Natural Science Foundation of Gansu Province, China (1308RJZA238) and HongLiu First-Class Disciplines Development Program of Lanzhou University of Technology.
- **Authors' contributions** Jinhuan Ma provides conceptualization, methodology, software, review, editing and verification. Zhiqiang Wei analyzed and explained the relevant photo-Fenton data. Qiang Lu provides some tests. Chao Li and Ling Li provide some ideas in writing the manuscript. Final manuscript read and approved by all authors.
- **Acknowledgements** The author thanks the supervisor for supporting this work, and the author also thanks the students of the research group for their help.

References

1. Amor C, De Torres-Socias E, Peres JA, Maldonado MI, Oller I, Malato S, & Lucas MS (2015) Mature landfill leachate treatment by coagulation/flocculation combined with Fenton and solar photo-Fenton processes. *J Hazard Mater* 286: 261-268. <https://doi.org/10.1016/j.jhazmat.2014.12.036>
2. Asadzadeh-Khaneghah S, Habibi-Yangjeh A, & Seifzadeh D (2018) Graphitic carbon nitride nanosheets coupled with carbon dots and BiOI nanoparticles: Boosting visible-light-driven photocatalytic activity. *J Taiwan Inst Chem E* 87: 98-111. <https://doi.org/10.1016/j.jtice.2018.03.017>
3. Asadzadeh-Khaneghah S, Habibi-Yangjeh A, Seifzadeh D, Chand H, & Krishnan V (2021) Visible-light-activated g-C₃N₄ nanosheet/carbon dot/FeOCl nanocomposites: Photodegradation of dye pollutants and tetracycline hydrochloride. *Colloid Surface A* 617. <https://doi.org/10.1016/j.colsurfa.2021.126424>
4. Chen CRR, Wang XDD, Wang SLL, Zhang JLL, & Tian BZZ (2020) Direct Z-Scheme Structure g-C₃N₄-BiOI with Highly Efficient Visible-Light-Driven Photocatalytic Activity for Bacteria Inactivation. *Chemistryselect* 5(47): 15084-15090. <https://doi.org/10.1002/slct.202003942>
5. Chen MD, Xu HM, Zhang XF, Li DY, & Xia DS (2018) Mechanism of heterogeneous activation of persulfate with FeOCl under visible light irradiation. *Journal of Materials Research* 33(21):3549-3558. <https://doi.org/10.1557/jmr.2018.246>
6. Chen YQ, Liu YP, Zhang L, Xie PC, Wang ZP, Zhou AJ, Fang Z, & Ma J (2018) Efficient degradation of imipramine by iron oxychloride-activated peroxymonosulfate process. *J Hazard Mater* 353:18-25. <https://doi.org/10.1016/j.jhazmat.2018.03.050>
7. Huang SP, Wei ZQ, Ma L, Li C, Lu Q, & Ma JH (2021). Hydrothermal synthesis, photo-electrochemical and photocatalytic activity of SnS₂/CdS nanocomposites. *J Mater Sci-mater EL* 32(1): 676-686. <https://doi.org/10.1007/s10854-020-04848-9>
8. Li C, Wei Z Q, Chen Y R, Ma L, Huang S P, Li L, & Ma J H (2021) Photo-electrochemical and enhanced photocatalytic activity of CdS/rGO nanocomposites prepared by hydrothermal method. *J Mater Sci-mater EL* 32(17): 22093-22105. <https://doi.org/10.1007/s10854-021-06679-8>

9. Li DY, Xiao Y, Pu MJ, Zan J, Zuo SY, Xu HM, & Xia DS (2019) A metal-free protonated g-C₃N₄ as an effective sodium percarbonate activator at ambient pH conditions: Efficiency, stability and mechanism. Mater Chem Phys 231: 225-232. <https://doi.org/10.1016/j.matchemphys.2019.04.016>
10. Li XR, Dai Y, Ma YD, Han SH, & Huang BB (2014) Graphene/g-C₃N₄ bilayer: considerable band gap opening and effective band structure engineering. Phys Chem Chem Phys 16(9): 4230-4235. <https://doi.org/10.1039/c3cp54592j>
11. Liu X, Zhang WY, Mao LQ, Yin Y, & Hu LC (2021) Synthesis of FeOCl-MoS₂ with excellent adsorption performance for methyl orange. J Mater Sci 56(11): 6704-6718. <https://doi.org/10.1007/s10853-020-05715-y>
12. Luo HW, Zeng YF, Cheng Y, He DQ, & Pan XL (2021) Activation of peroxymonosulfate by iron oxychloride with hydroxylamine for ciprofloxacin degradation and bacterial disinfection. Sci Total Environ 799. <https://doi.org/10.1016/j.scitotenv.2021.149506>
13. Luo JM, Sun M, Ritt CL, Liu X, Pei Y, Crittenden JC, & Elimelech M (2019) Tuning Pb(II) Adsorption from aqueous solutions on ultrathin iron oxychloride (FeOCl) nanosheets. Environ Sci Technol 53(4): 2075-2085. <https://doi.org/10.1021/acs.est.8b07027>
14. Ma JH, Wei ZQ, Li L, Ma L, Li C, & Huang SP (2021) Synthesis and photoelectrochemical properties of visible-light response g-C₃N₄@CdS heterojunctions photocatalyst. Desalin Water Treat 231: 287-296. <https://doi.org/10.5004/dwt.2021.27488>
15. Ma JQ, Yang QF, Wen YZ, & Liu WP (2017) Fe-g-C₃N₄/graphitized mesoporous carbon composite as an effective Fenton-like catalyst in a wide pH range. Applied Catalysis B-Environmental 201: 232-240. <https://doi.org/10.1016/j.apcatb.2016.08.048>
16. Ma YP, Wang JD, Zhang XJ, Zhang XB, Mu BL., & Zhang, H. Z. (2021). Enhancement of Hg-0 oxidation removal in chloride-free flue gas over FeOCl-modified commercial selective catalytic reduction catalyst. Colloid Interfac Sci 44, 100472. <https://doi.org/10.1016/j.colcom.2021.100472>
17. Nguyen TTH, Le MC, & Ha NN (2021) Understanding the influence of single metal (Li, Mg, Al, Fe, Ag) doping on the electronic and optical properties of g-C₃N₄: a theoretical study. Molecular Simulation 47(1): 10-17. <https://doi.org/10.1080/08927022.2020.1858078>
18. Nguyen VH, Mousavi M, Ghasemi JB, Le QV, Delbari SA, Asl MS, Shokouhimehr M, Mohammadi M, Azizian-Kalandaragh Y, & Namini AS (2021) In situ preparation of g-C₃N₄ nanosheet/FeOCl: Achievement and promoted photocatalytic nitrogen fixation activity. Colloid Interfac Sci 587: 538-549. <https://doi.org/10.1016/j.jcis.2020.11.011>
19. Pan XY, Fan XK, Liang AP, Zhang SQ, Wang WH, Qu SY, & Li CL (2021) Electron-rich CNTs modified FeOCl/Fe(2)O₃ with improved Fenton catalytic performance. Composites Communications 27: 100811. <https://doi.org/10.1016/j.coco.2021.100811>
20. Qu LH, Deng ZY, Yu J, Lu XK, Zhong CG, Zhou PX, Lu TS, Zhang JM, & Fu XL (2020) Mechanical and electronic properties of graphitic carbon nitride (g-C₃N₄) under biaxial. Vacuum 176:109358. <https://doi.org/10.1016/j.vacuum.2020.109358>

21. Qu SY, Li CL, Sun X, Wang JW, Luo HJ, Wang S, Ta JY, & Li DY (2019) Enhancement of peroxymonosulfate activation and utilization efficiency via iron oxychloride nanosheets in visible light. *Sep Purif Technol* 224: 132-141. <https://doi.org/10.1016/j.seppur.2019.04.084>
22. Qu SY, Wang WH, Pan XY, & Li CL (2020) Improving the Fenton catalytic performance of FeOCl using an electron mediator. *J Hazard Mater* 384: 121494. <https://doi.org/10.1016/j.jhazmat.2019.121494>
23. Ren HT, Jia SY, Wu SH, Zhang TH, & Han X (2015) Phase transformation synthesis of novel $\text{Ag}_2\text{O}/\text{Ag}_2\text{CO}_3/\text{g-C}_3\text{N}_4$ composite with enhanced photocatalytic activity. *Materials Letters*, 142: 15-18. <https://doi.org/10.1016/j.matlet.2014.11.082>
24. Sabri M, Habibi-Yangjeh A, Chand H, & Krishnan V (2020) Activation of persulfate by novel $\text{TiO}_2/\text{FeOCl}$ photocatalyst under visible light: Facile synthesis and high photocatalytic performance. *Sep Purif Technol* 250: 117268. <https://doi.org/10.1016/j.seppur.2020.117268>
25. Sun M, Chu CH, Geng FL, Lu XL, Qu JH, Crittenden J, Elimelech M, & Kim JH (2018) Reinventing Fenton Chemistry: Iron oxychloride nanosheet for pH-insensitive H_2O_2 activation. *Environ Sci Tech Let* 5(3): 186-191. <https://doi.org/10.1021/acs.estlett.8b00065>
26. Varaprasad HS, Sridevi PV, & Anuradha MS (2021) Optical, morphological, electrical properties of $\text{ZnO-TiO}_2\text{-SnO}_2/\text{CeO}_2$ semiconducting ternary nanocomposite. *Adv Powder Technol* 32(5): 1472-1480. <https://doi.org/10.1016/j.appt.2021.02.042>
27. Wei ZQ, Huang SP, Zhang XD, Lu CG, & He YJ (2020) Hydrothermal synthesis and photo-Fenton degradation of magnetic $\text{MnFe}_2\text{O}_4/\text{rGO}$ nanocomposites. *J Mater Sci-mater EL* 31(7): 5176-5186. <https://doi.org/10.1007/s10854-020-03077-4>
28. Xing WX, Zhou L, Chen B, Lei JY, Wang LZ, & Zhang JL (2020) $\alpha\text{-FeOOH-MoO}_3$ nanorod for effective photo-fenton degradation of dyes and antibiotics at a wide range of pH. *Chem-Asian J* 15(17): 2749-2753. <https://doi.org/10.1002/asia.202000668>
29. Yang H (2021) A short review on heterojunction photocatalysts: Carrier transfer behavior and photocatalytic mechanisms. *Mater Res Bull* 142: 111406. <https://doi.org/10.1016/j.materresbull.2021.111406>
30. Yang XJ, Xu XM, Xu XC, Xu J, Wang HL, Semiat R, & Han YF (2016) Modeling and kinetics study of Bisphenol A (BPA) degradation over an $\text{FeOCl}/\text{SiO}_2$ Fenton-like catalyst. *Catalysis Today* 276: 85-96. <https://doi.org/10.1016/j.cattod.2016.01.002>
31. Yao TJ, Jia WJ, Feng Y, Zhang JS, Lian YF, Wu J, & Zhang X (2019) Preparation of reduced graphene oxide nanosheet/ Fe_xO_y /nitrogen-doped carbon layer aerogel as photo-Fenton catalyst with enhanced degradation activity and reusability. *J Hazard Mater* 362: 62-71. <https://doi.org/10.1016/j.jhazmat.2018.08.084>
32. Ye YC, Yang H, Wang XX, & Feng WJ (2018). Photocatalytic, Fenton and photo-Fenton degradation of RhB over Z-scheme $\text{g-C}_3\text{N}_4/\text{LaFeO}_3$ heterojunction photocatalysts. *Mat Sci Semicon Proc* 82: 14-24. <https://doi.org/10.1016/j.mssp.2018.03.033>

33. Zeng HM, Liu YL, Xu ZG, Wang Y, Chai YQ, Yuan R, & Liu H Y (2019) Construction of a Z-scheme g-C₃N₄/Ag/AgI heterojunction for highly selective photoelectrochemical detection of hydrogen sulfide. *Chemical Communications* 55(79): 11940-11943. <https://doi.org/10.1039/c9cc05356e>
34. Zhao JZ, Ji MX, Di J, Zhang Y, He MQ, Li HM, & Xia JX (2020) Novel Z-scheme heterogeneous photo-Fenton-like g-C₃N₄/FeOCl for the pollutants degradation under visible light irradiation. *J Photoch Photobio A* 391:112343. <https://doi.org/10.1016/j.jphotochem.2019.112343>
35. Zheng JH, & Zhang L (2018) Incorporation of CoO nanoparticles in 3D marigold flower-like hierarchical architecture MnCo₂O₄ for highly boosting solar light photo-oxidation and reduction ability. *Appl Catal B-Environ* 237: 1-8. <https://doi.org/10.1016/j.apcatb.2018.05.060>
36. Zhu YF, Ma SC, Yang Y, Li JQ, Mei YQ, Liu L, Yao TJ, & Wu J (2021) Direct Z-scheme Fe₂(MoO₄)₃/MoO₃ heterojunction: Photo-Fenton reaction and mechanism comprehension. *J Alloy Compd*, 873: 159830. <https://doi.org/10.1016/j.jallcom.2021.159830>

Figures

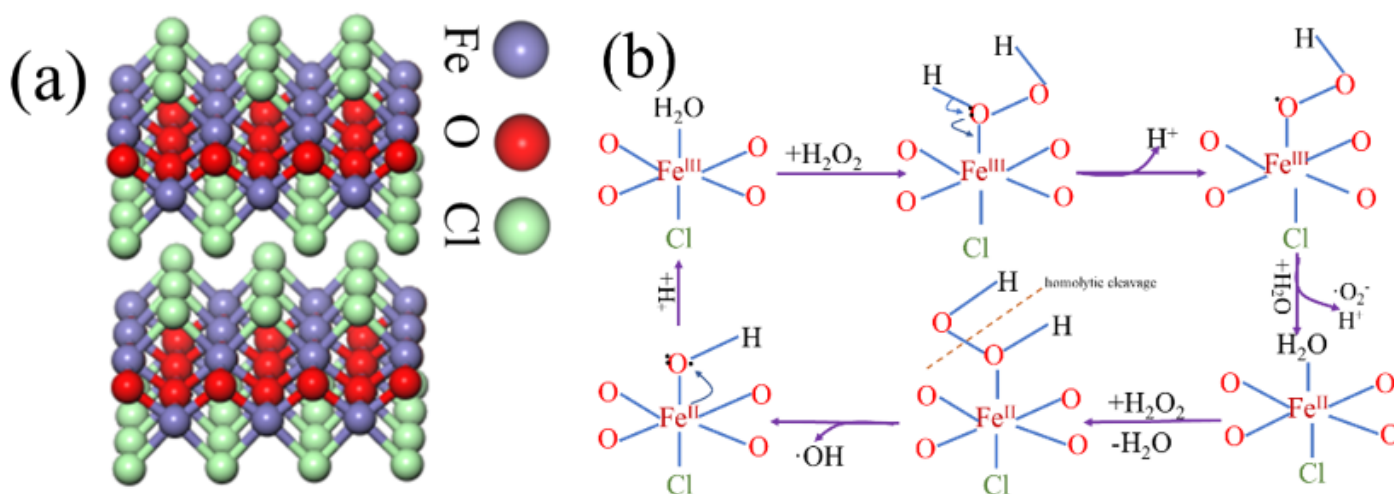


Figure 1

(a) Layered crystal structure of FeOCl (b) Fe(II)-Fe(III) and H₂O₂ reaction cycle diagram in FeOCl nanosheets (Sun et al., 2018)

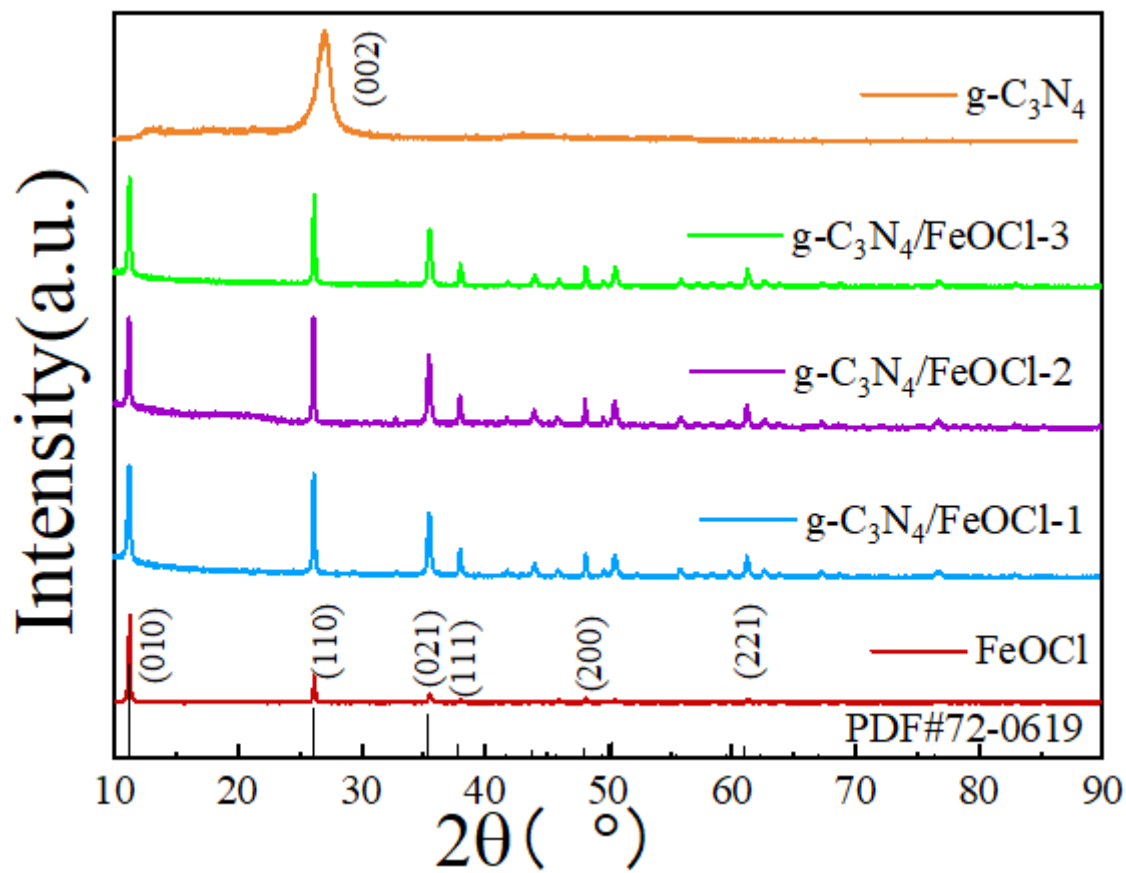


Figure 2

XRD patterns of pure FeOCl , pure $\text{g-C}_3\text{N}_4$, and $\text{g-C}_3\text{N}_4/\text{FeOCl}$ composites

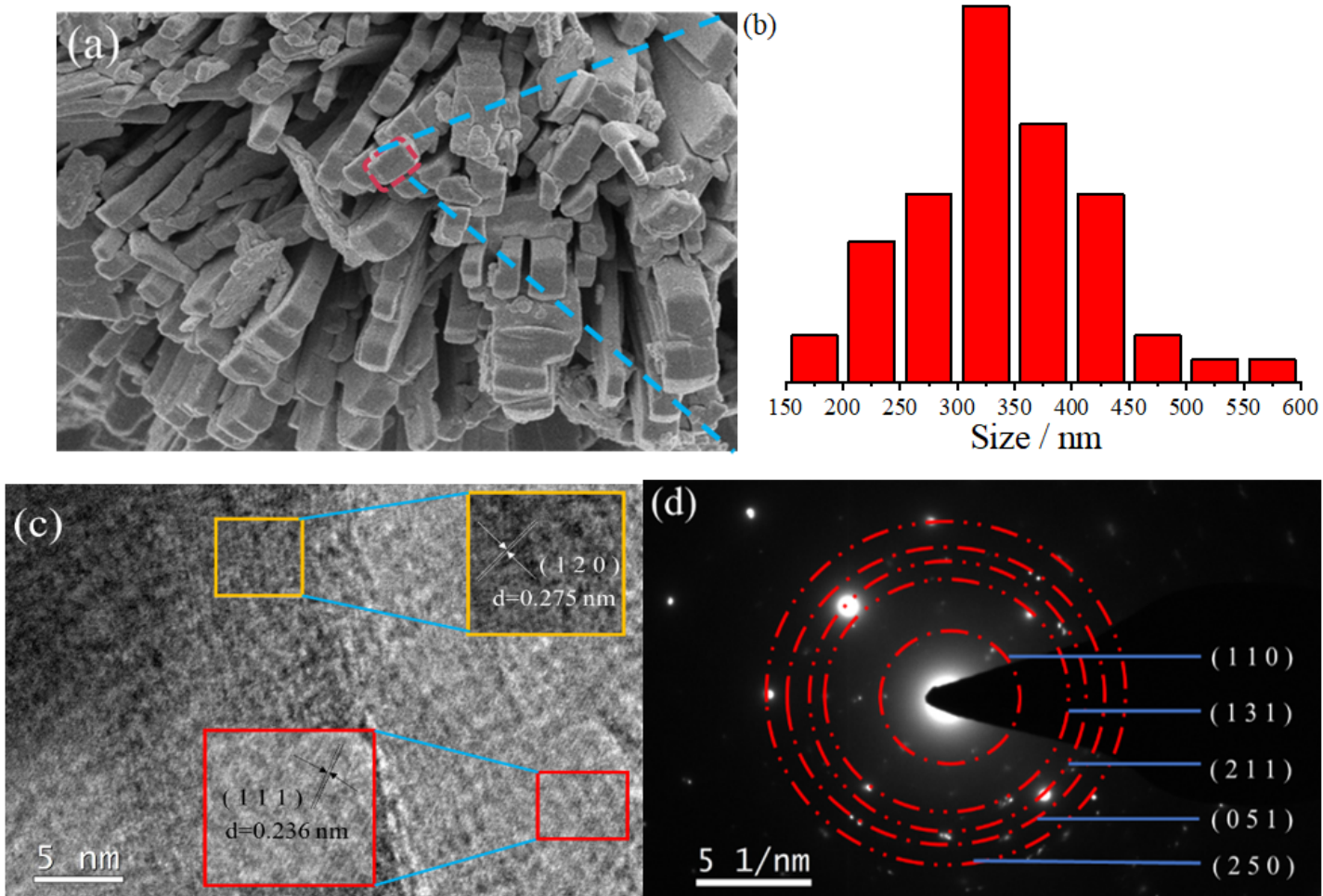


Figure 3

(a,b) SEM and Particle size images of FeOCl, (c,d) HRTEM and Selected Area Electron Diffraction images of g-C₃N₄/FeOCl-2

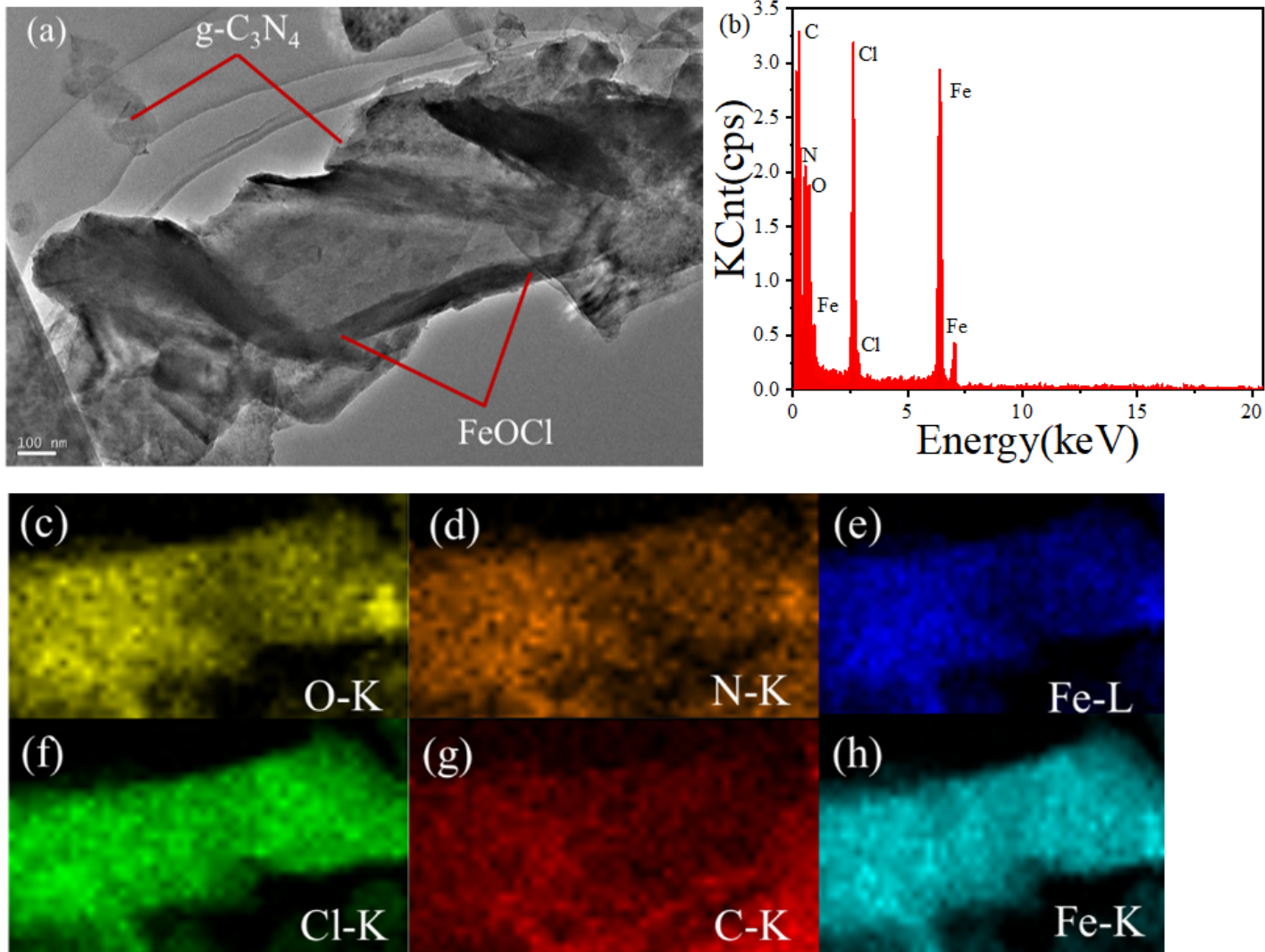


Figure 4

(a) TEM, (b) EDX and (c~h) TEM-Mapping spectra of g-C₃N₄/FeOCl-2

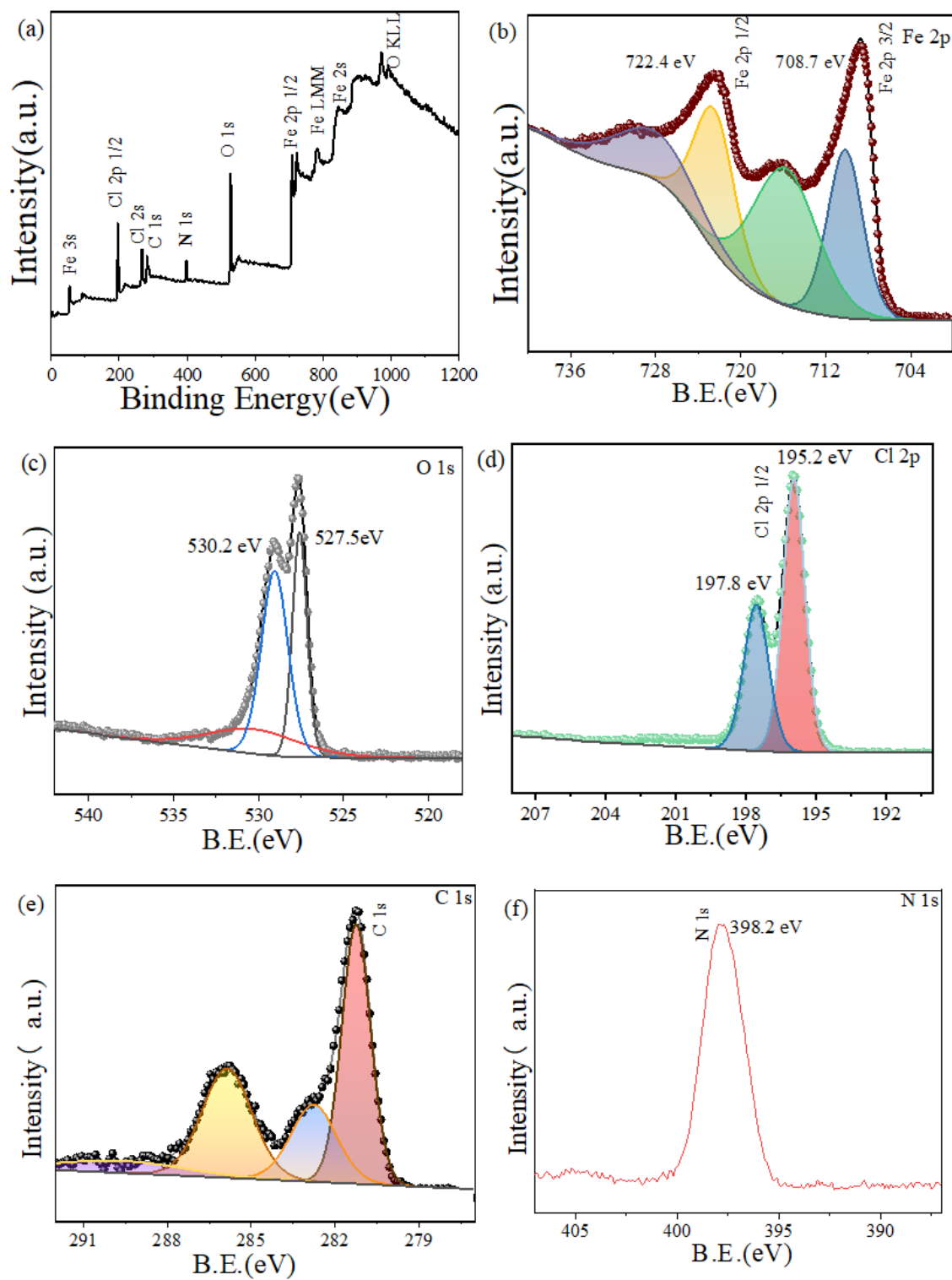


Figure 5

(a) XPS survey spectra and (b) also XPS spectra of Fe 2p, (c) O 1s, (d) Cl 2p, (e) C 1s, and (f) N 1s in the g-C₃N₄/FeOCl-2

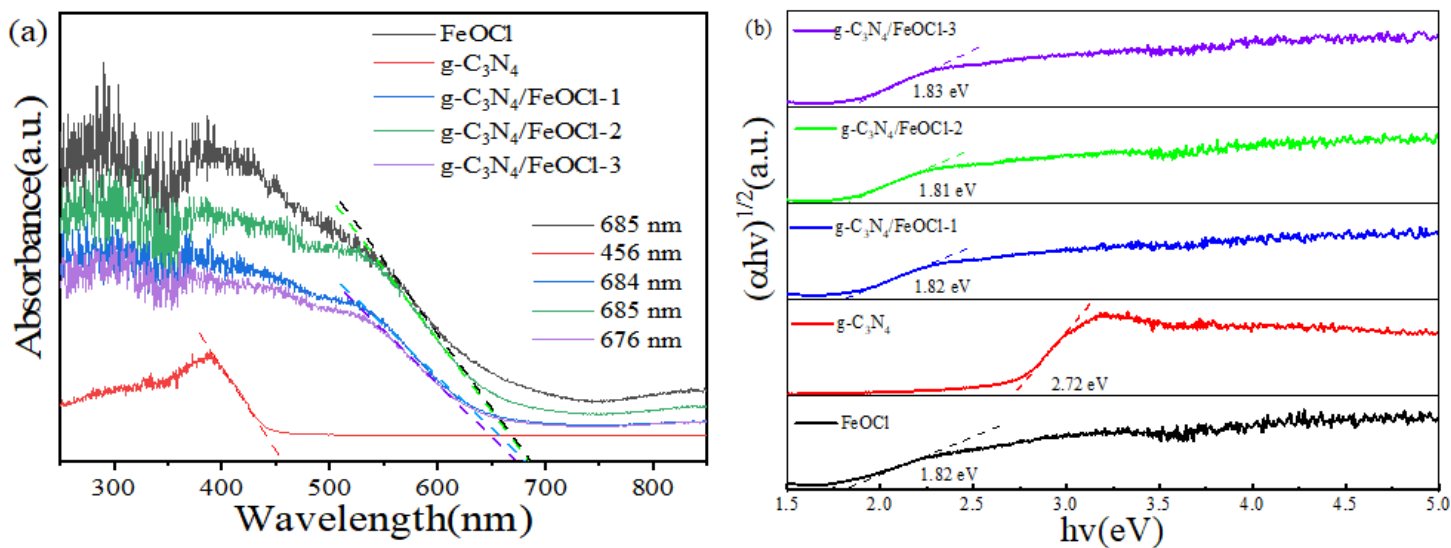


Figure 6

(a) UV-vis absorption spectra and (b) the $(\alpha h\nu)^2$ versus $h\nu$ curve of pure FeOCl, pure g-C₃N₄, and g-C₃N₄/FeOCl composites

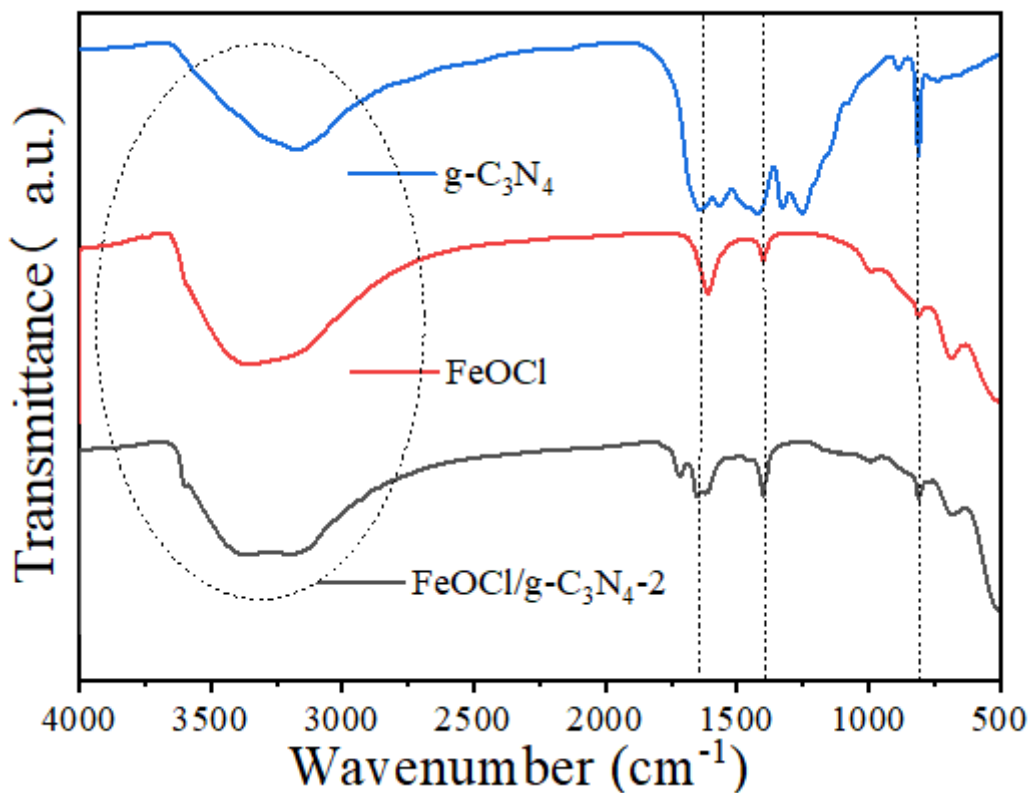


Figure 7

FT-IR images of the pure FeOCl, pure g-C₃N₄, and g-C₃N₄/FeOCl-2

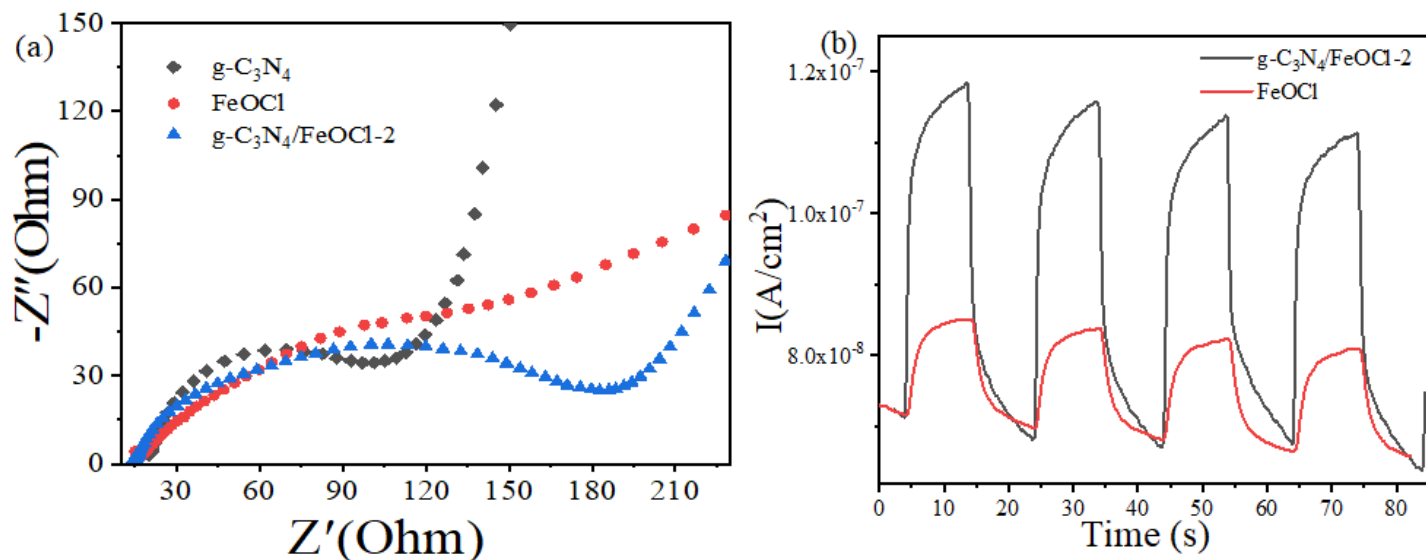


Figure 8

(a) Electrochemical impedance spectroscopy and (b) transient photocurrent responses of pure FeOCl and $g-C_3N_4/FeOCl-2$ samples.

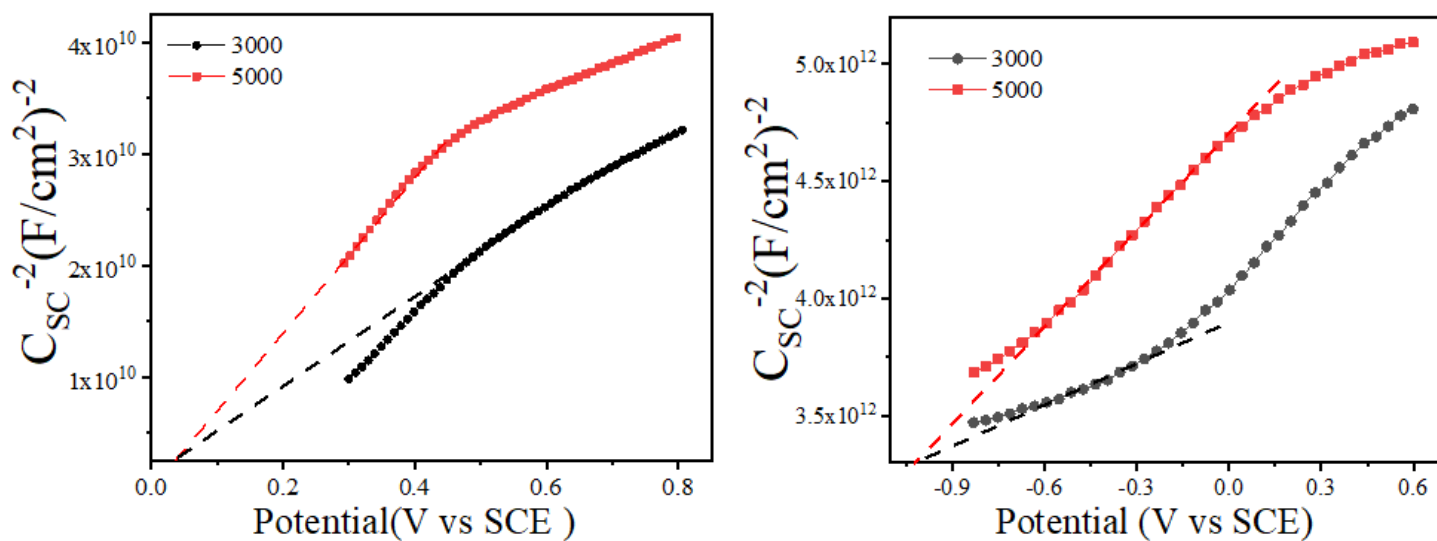


Figure 9

(a, b) M-S plots of pure FeOCl and $g-C_3N_4$

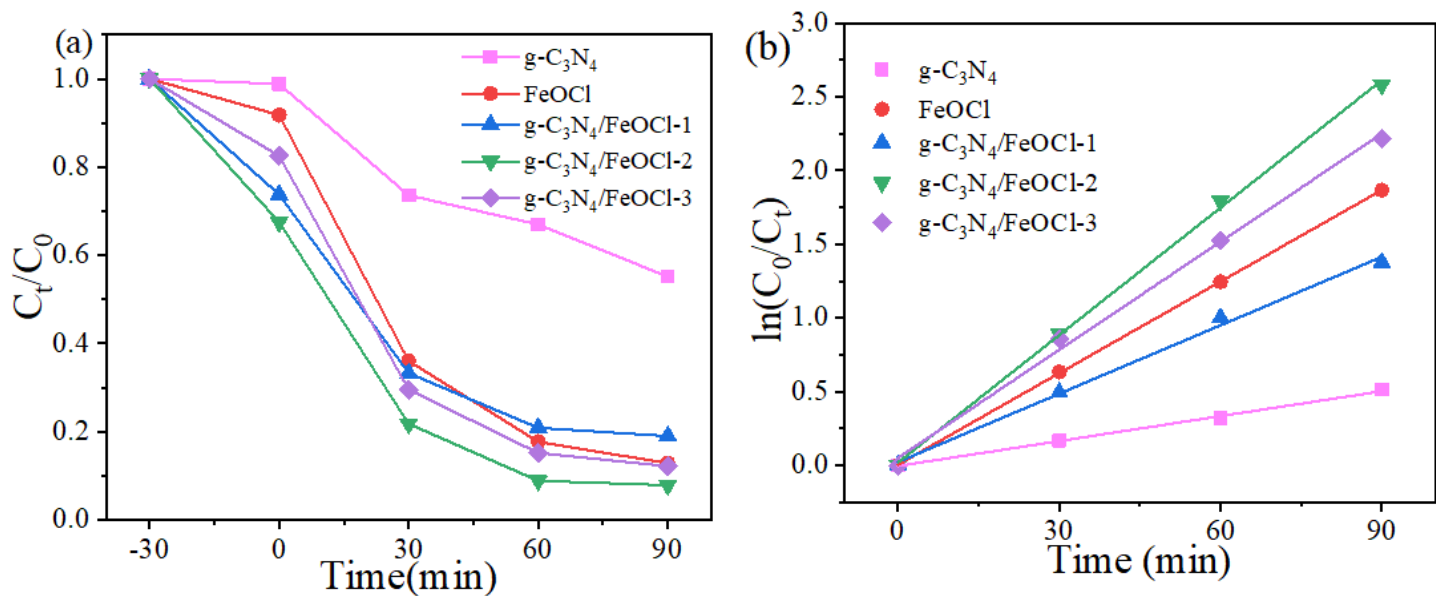


Figure 10

(a) The photocatalytic degradation of RhB over time and (b) plots of $\ln(C_t/C_0)$ vs irradiation time for FeOCl and g-C₃N₄/FeOCl samples

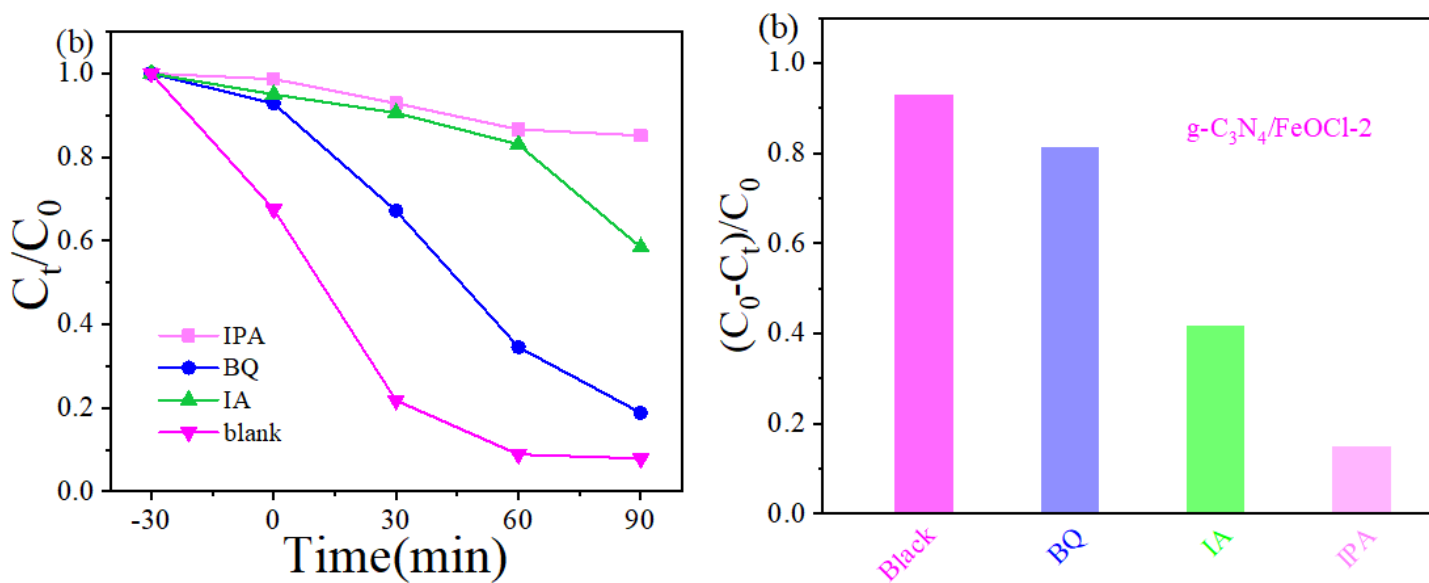


Figure 11

(a) radical-trapping experiment and (b) the degradation rate of RhB under photo-Fenton catalyst g-C₃N₄/FeOCl-2

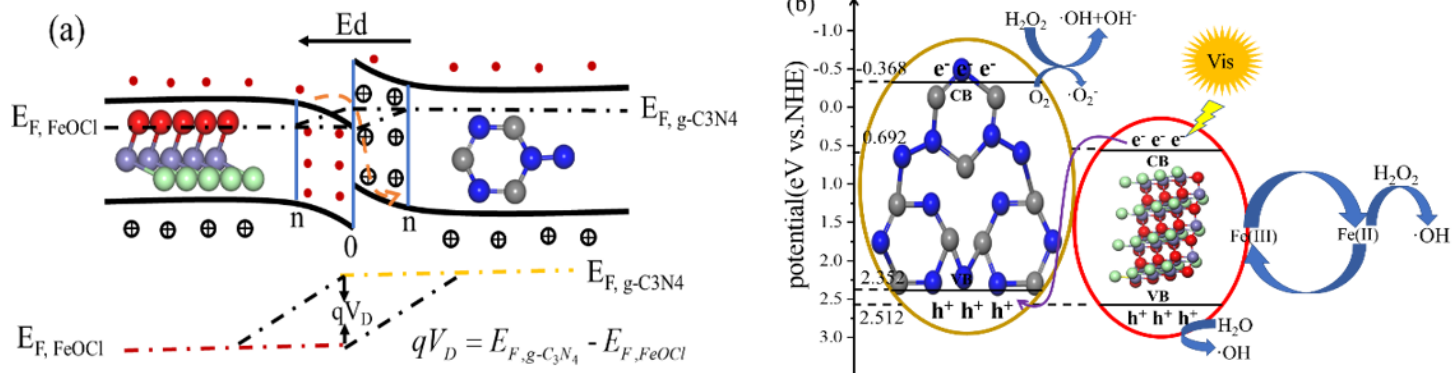


Figure 12

(a) Band diagram of n-n type heterojunction and (b) the schematic diagram of photo-Fenton mechanism of g-C₃N₄/FeOCl-2